

Finite-element simulations of Stoneley guided-wave reflection and scattering at the tips of fluid-filled fractures

Marcel Frehner¹ and Stefan M. Schmalholz²

ABSTRACT

The reflection and scattering of Stoneley guided waves at the tip of a crack filled with a viscous fluid was studied numerically in two dimensions using the finite-element method. The rock surrounding the crack is fully elastic and the fluid filling the crack is elastic in its bulk deformation behavior and viscous in its shear deformation behavior. The crack geometry, especially the crack tip, is resolved in detail by the unstructured finite-element mesh. At the tip of the crack, the Stoneley guided wave is reflected. The amplitude ratio between reflected and incident Stoneley guided wave is calculated from numerical simulations, which provide values ranging between 43% and close to 100% depending on the type of fluid filling the crack (water, oil or hydrocarbon gas), the crack geometry (elliptical or rectangular), and the presence of a

small gas cap at the cracktip. The interference of incident and reflected Stoneley guided waves leads to a node (zero amplitude) at the tip of the crack. At other positions along the crack, this interference increases the amplitude. However, the exponential decay away from the crack makes the Stoneley guided wave difficult to detect at a relatively short distance away from the crack. The part of the Stoneley guided wave that is not reflected is scattered at the crack tip and emitted into the surrounding elastic rock as body waves. For fully saturated cracks, the radiation pattern of these elastic body waves points in every direction from the crack tip. The emitted elastic body waves can allow the detection of Stoneley guided wave-related resonant signals at distances away from the crack where the amplitude of the Stoneley guided wave itself is too small to be detected.

INTRODUCTION

Fractures in rocks are of great practical interest not only because they contribute significantly to the permeability of a rock (e.g., [Faoro et al., 2009](#)) but also because they can have a significant influence on seismic waves that pass through fractured rocks. For example, [Saenger and Shapiro \(2002\)](#) show with numerical simulations that the wave velocity of body waves decreases drastically with increasing crack density, [Groenenboom and Falk \(2000\)](#) model numerically and measure in the laboratory that scattering of body waves at hydraulic fractures is strong enough to determine the fracture dimensions, and [Kostek et al. \(1998\)](#) and [Ionov \(2007\)](#) show that fractures intersecting a borehole can have a major impact in seismic surveys. One phenomenon of particular interest are Stoneley guided waves (SGW), a highly dispersive and slowly propagating wave mode that is bound to a crack (e.g., [Ferrazzini and Aki, 1987](#);

[Ashour, 2000](#); [Korneev, 2008](#)). SGWs also are referred to as crack waves ([Chouet, 1986](#); [Yamamoto and Kawakatsu, 2008](#)), slow Stoneley waves ([Ferrazzini and Aki, 1987](#)) or simply Stoneley waves in a fracture ([Ashour, 2000](#)). They are of interest because of their ability to develop a resonance when propagating back and forth along a crack, which “should lead to strongly frequency dependent propagation effects for seismic waves” ([Korneev, 2008](#)). Despite their potential importance for wave propagation in porous and fractured rocks, SGWs are not considered in existing effective medium and poroelastic theories, such as the Hudson model ([Hudson, 1980, 1981](#)), the squirt-flow model ([Mavko and Jizba, 1991](#); [Dvorkin et al., 1995](#)) or the Biot model ([Biot, 1962](#)). Analytical studies of SGW propagation are available only for infinite straight cracks ([Ferrazzini and Aki, 1987](#); [Ashour, 2000](#); [Korneev, 2008](#)) not taking into account the reflection and scattering at crack tips and therefore also not taking into account the resonant behavior of SGWs. Numerical stud-

Presented at the 78th Annual International Meeting, SEG.

Manuscript received by the Editor 16 February 2009; revised manuscript received 26 June 2009; published online 23 March 2010.

¹Formerly ETH Zurich, Department of Earth Sciences, Geological Institute, Zurich, Switzerland; presently University of Vienna, Department for Geodynamics and Sedimentology, Vienna, Austria. E-mail: marcel.frehner@univie.ac.at.

²Formerly ETH Zurich, Geological Institute, Department of Earth Sciences, Zurich, Switzerland; presently University of Lausanne, Institute of Geology and Palaeontology, Lausanne, Switzerland. E-mail: stefan.schmalholz@unil.ch.

© 2010 Society of Exploration Geophysicists. All rights reserved.

ities are rare (e.g., Chouet, 1986; Yamamoto and Kawakatsu, 2008) and available only for simple crack geometries (usually rectangular). This paper extends this body of knowledge by studying the propagation, reflection, and scattering of SGWs at crack tips of different shapes and with a high numerical resolution.

Because SGWs are bound to a crack, they are reflected at the crack tip and can propagate back and forth along a crack. The resulting resonance caused by SGWs propagating in finite fractures is used by Aki et al. (1977), Chouet (1988), and Chouet (1996) to explain long-period volcanic tremor signals that are observed before volcanic eruptions and potentially can be used for eruption forecasting. The reflection coefficient at the crack tip together with the attenuation determines how many times an SGW can propagate back and forth along a crack and, therefore, how well it can develop a resonance. Knowing that SGWs cannot be detected at a relatively short distance away from the crack due to the exponential decay of their amplitude (Ferrazzini and Aki, 1987), the way the tremor signal is transmitted to recording stations at the earth's surface remained unclear. Ferrazzini and Aki (1987) suspect that "reflection at the crack tip should provide an important source of radiation in the case of a finite crack." However, the reflection of SGWs at the crack tip and the corresponding radiation of body waves from the crack tip have not been investigated in detail until now, which is why they are the main subject of this paper. The part of the SGW that is not reflected is scattered at the crack tip and P- and S-waves are radiated away from the crack tip. The radiation pattern of these P- and S-waves is of great importance for measuring the resonant behavior of the SGW (i.e., the tremor signal). Similar to volcanic areas, SGWs can be of great importance in fractured reservoirs. Frequency-dependent wave-propagation phenomena in exploration seismology can help to characterize subsurface fractured reservoirs.

The study of SGWs is a multiscale problem where typical wavelengths can be orders of magnitudes larger than the characteristic size of the cracks. For numerical simulations, this "presents a major computational challenge" (Korneev, 2008). The standard numerical method for simulating wave propagation in fractured media is the finite-difference method (FDM) using a rectangular numerical grid (Chouet, 1986; Kostek et al., 1998; Groenenboom and Falk, 2000; Saenger and Shapiro, 2002; Krüger et al., 2005). The numerical method used in this study is the finite-element method (FEM) (e.g., Zienkiewicz and Taylor, 2000; Cohen, 2002) using an unstructured numerical mesh. A similar method also using an unstructured mesh is, for example, the discontinuous Galerkin method described by Käser and Dumbser (2008). The unstructured mesh allows resolving geometrically complex objects with strong material contrast (e.g., the tip of a crack) very finely and accurately without the need to have a high resolution elsewhere in the domain (Frehner et al., 2008).

In contrast, rectangular grids always approximate objects in a staircase-like way, which leads to numerical inaccuracies no matter how fine the numerical grid is. For time integration in wave-propagation simulations, explicit schemes are most common. The largest explicit time increment allowed for stable numerical solutions is determined by the smallest spatial resolution and the largest wave velocity in the domain (Virieux, 1986; Higham, 1996; Saenger et al., 2000). Both parameters take extreme values when SGWs are simulated. Spatial resolution needs to be very fine around the crack tip and the dispersive P-waves in the viscous fluid have a velocity tending to infinity for very high frequencies. Small-amplitude numerical errors or noise, which is commonly characterized by high frequencies, can grow during the simulations and lead to numerical instabil-

ities. One possibility to avoid these instabilities in viscous fluids is defining frequency-dependent material parameters (Saenger et al., 2005), which allows defining the high-frequency limit of the dispersive waves from infinity down to a finite value. The alternative used in this study is an implicit time-integration method (e.g., Chen et al., 2008; Frehner et al., 2008), which does not require fulfilling any stability criterion. Material parameters in the numerical algorithm can be implemented exactly the same way they are written in the constitutive equations and do not have to be made frequency dependent.

The paper begins with a description of the mathematical and geometrical model. Properties of the SGW as a function of the model setup and the different fluids used in this study are described using analytical expressions of Ferrazzini and Aki (1987) and Korneev (2008). A brief introduction to the applied two-dimensional (2D) FEM is given before the numerical results are shown. The reflection of an SGW at the tip of a crack is quantified as a function of crack geometry and the type of fluid filling the crack. The radiation pattern of elastic body waves that are emitted into the surrounding rock is described in detail. The paper ends with simulations for two advanced model setups (two intersecting fractures and fractures filled with two different fluids) and a discussion about applicability of the modeling results to natural environments.

MODEL

The propagation of SGWs is studied with a 2D model with Cartesian coordinates x and y . The mathematical description and the geometrical setup are described below.

Mathematical model

The 2D formulation used here is a plane-strain approximation of the full 3D formulation, i.e., all spatial derivatives in the third dimension, the out-of-plane displacement, and all out-of-plane strains are equal to zero. However, the out-of-plane normal stress is allowed to have a finite value, which depends only on the two in-plane normal strains. The plane-strain approximation in 2D is equivalent to a 3D formulation with geometries extending to infinity in the third dimension (i.e., all material parameters are constant in the third dimension). For this formulation, standard material parameters can be used that are defined in 3D (e.g., elastic bulk modulus K). A full 3D formulation is computationally expensive and is not used in this study. Results obtained with the 2D plane-strain formulation are applicable to cracks with a relatively round crack surface (i.e., penny-shaped cracks) but not to strongly elongated cracks (i.e., cigar-shaped cracks).

The force-balance equation (or conservation of linear momentum) that describes the state of the acting forces in 2D (Love, 1927; Lindsay, 1960; Achenbach, 1973; Shames and Cozzarelli, 1997; Aki and Richards, 2002; Pujol, 2003) is given by

$$\rho \underbrace{\begin{Bmatrix} \ddot{u}_x \\ \ddot{u}_y \end{Bmatrix}}_{\ddot{\mathbf{u}}} = \underbrace{\begin{bmatrix} \frac{\partial}{\partial x} & 0 & \frac{\partial}{\partial y} \\ 0 & \frac{\partial}{\partial y} & \frac{\partial}{\partial x} \end{bmatrix}}_{\mathbf{B}^T} \underbrace{\begin{Bmatrix} \sigma_{xx} \\ \sigma_{yy} \\ \sigma_{xy} \end{Bmatrix}}_{\boldsymbol{\sigma}}, \quad (1)$$

where ρ is density and $\ddot{\mathbf{u}}$ is the second time derivative of the displacement vector. The symbol \sim denotes the continuous nature of $\ddot{\mathbf{u}}$ (not yet discretized with any numerical method). Vector $\boldsymbol{\sigma}$ contains the

three independent components σ_{ij} of the symmetric total stress tensor (i.e., σ_{xx} , σ_{yy} , and σ_{xy}). Compressive stresses are defined as negative. Superscript T denotes the transpose of a matrix. The deformation behavior of the medium is divided into a bulk (or volumetric) part and a deviatoric (or shear) part. Therefore, the vector $\boldsymbol{\sigma}$ is also divided into a bulk and a deviatoric part (Shames and Cozzarelli, 1997):

$$\begin{Bmatrix} \sigma_{xx} \\ \sigma_{yy} \\ \sigma_{xy} \end{Bmatrix} = \begin{Bmatrix} -p \\ -p \\ 0 \end{Bmatrix} + \underbrace{\begin{Bmatrix} s_{xx} \\ s_{yy} \\ s_{xy} \end{Bmatrix}}_{\mathbf{s}}. \quad (2)$$

Vector \mathbf{s} contains the three independent components s_{ij} of the symmetric deviatoric stress tensor and p is pressure (or mean stress). Vector $\boldsymbol{\varepsilon}$, containing the three independent components (i.e., two normal components ε_{xx} and ε_{yy} , and one shear component γ_{xy}) of the symmetric total strain tensor, is divided into a bulk and a deviatoric part in a similar way:

$$\underbrace{\begin{Bmatrix} \varepsilon_{xx} \\ \varepsilon_{yy} \\ \gamma_{xy} \end{Bmatrix}}_{\boldsymbol{\varepsilon}} = \begin{Bmatrix} \partial u_x / \partial x \\ \partial u_y / \partial y \\ \partial u_x / \partial y + \partial u_y / \partial x \end{Bmatrix} = \begin{Bmatrix} \Theta / 3 \\ \Theta / 3 \\ 0 \end{Bmatrix} + \underbrace{\begin{Bmatrix} e_{xx} \\ e_{yy} \\ g_{xy} \end{Bmatrix}}_{\mathbf{e}}. \quad (3)$$

Vector \mathbf{e} contains the three independent components (i.e., two normal components e_{xx} and e_{yy} , and one shear component g_{xy}) of the symmetric deviatoric strain tensor and Θ is the bulk strain (i.e., $\varepsilon_{xx} + \varepsilon_{yy} + \varepsilon_{zz}$, where ε_{zz} is equal to zero due to the plain-strain formulation). Two different types of media are considered in this study: the rock (solid, superscript s) and the fluid (superscript f) that fills the crack. The behavior of both media is the same as in Korneev (2008). The bulk deformation behavior of both media is linear elastic, while the deviatoric deformation behavior of the two media is different. The deviatoric deformation of the solid rock is linear elastic and that of the fluid is linear viscous. The constitutive equation for the elastic bulk deformation of both media is

$$-p = K^{s,f} \Theta, \quad (4)$$

where $K^{s,f}$ is the elastic bulk modulus of the solid and the fluid, respectively. The constitutive equation for the deviatoric deformation of the elastic solid is

$$\begin{Bmatrix} s_{xx} \\ s_{yy} \\ s_{xy} \end{Bmatrix} = \begin{bmatrix} 2\mu & 0 & 0 \\ 0 & 2\mu & 0 \\ 0 & 0 & \mu \end{bmatrix} \begin{Bmatrix} e_{xx} \\ e_{yy} \\ g_{xy} \end{Bmatrix}, \quad (5)$$

where μ is the elastic shear modulus. The constitutive equation for the viscous deviatoric deformation of the fluid is

$$\begin{Bmatrix} s_{xx} \\ s_{yy} \\ s_{xy} \end{Bmatrix} = \begin{bmatrix} 2\eta & 0 & 0 \\ 0 & 2\eta & 0 \\ 0 & 0 & \eta \end{bmatrix} \underbrace{\begin{Bmatrix} \dot{e}_{xx} \\ \dot{e}_{yy} \\ \dot{g}_{xy} \end{Bmatrix}}_{\dot{\mathbf{e}}}, \quad (6)$$

where η is the shear viscosity. Vector $\dot{\mathbf{e}}$ is the time derivative of vector \mathbf{e} . The formulation for total stress in the elastic solid is found by combining equations 2–5 as

$$\begin{Bmatrix} \sigma_{xx} \\ \sigma_{yy} \\ \sigma_{xy} \end{Bmatrix} = \begin{bmatrix} K^s + 4\mu/3 & K^s - 2\mu/3 & 0 \\ K^s - 2\mu/3 & K^s + 4\mu/3 & 0 \\ 0 & 0 & \mu \end{bmatrix} \times \begin{Bmatrix} \partial \tilde{u}_x / \partial x \\ \partial \tilde{u}_y / \partial y \\ \partial \tilde{u}_x / \partial y + \partial \tilde{u}_y / \partial x \end{Bmatrix}. \quad (7)$$

The formulation for total stress in the fluid is found by combining equations 2–4 and 6 as

$$\begin{Bmatrix} \sigma_{xx} \\ \sigma_{yy} \\ \sigma_{xy} \end{Bmatrix} = \begin{bmatrix} K^f & K^f & 0 \\ K^f & K^f & 0 \\ 0 & 0 & 0 \end{bmatrix} \begin{Bmatrix} \partial \tilde{u}_x / \partial x \\ \partial \tilde{u}_y / \partial y \\ \partial \tilde{u}_x / \partial y + \partial \tilde{u}_y / \partial x \end{Bmatrix} + \begin{bmatrix} 4\eta/3 & -2\eta/3 & 0 \\ -2\eta/3 & 4\eta/3 & 0 \\ 0 & 0 & \eta \end{bmatrix} \begin{Bmatrix} \partial \dot{\tilde{u}}_x / \partial x \\ \partial \dot{\tilde{u}}_y / \partial y \\ \partial \dot{\tilde{u}}_x / \partial y + \partial \dot{\tilde{u}}_y / \partial x \end{Bmatrix}. \quad (8)$$

Equation 7 describes the stress-strain relation of a fully elastic medium in 2D where both the bulk and shear deformation behavior are elastic. Therefore, P- and S-waves can propagate in such a medium without velocity dispersion or attenuation. Equation 8 describes the stress-strain relation of a so-called viscoacoustic medium (a viscous fluid) in 2D. Only the bulk deformation behavior is elastic, while the shear deformation behavior is viscous. Therefore, shear waves exist exclusively due to viscosity and have a diffusive character. On the other hand, P-waves can propagate in such a medium but they are attenuated by the viscous damping terms. The formulation is very similar to the one-dimensional formulation of a medium using a Kelvin-Voigt model (Bourbie et al., 1987; Carcione, 2001). The P-wave phase velocity in the fluid V_p^f is dispersive with a low-frequency limit equal to $V_C = \sqrt{K^f / \rho^f}$. For increasing frequency, the phase velocity increases continuously and tends to infinity without having a high-frequency limit. The quality factor for P-waves in such a viscoacoustic fluid Q_p^f is equal to infinity (no attenuation) in the low-frequency limit and $Q_p^f = 0$ (purely diffusive propagation type) in the high-frequency limit. Setting the shear viscosity η to 0 leads to a purely acoustic formulation, also called an inviscid fluid. P-waves in an inviscid fluid propagate with the velocity V_C . They are neither dispersive nor attenuated. Equations 7 and 8 can be written in a more general way as

$$\boldsymbol{\sigma} = \mathbf{D}_{el} \boldsymbol{\varepsilon} + \mathbf{D}_{visc} \dot{\boldsymbol{\varepsilon}}, \quad (9)$$

where, in the purely elastic case, \mathbf{D}_{el} is the matrix given in equation 7 and \mathbf{D}_{visc} is equal to 0. In the viscoacoustic case, \mathbf{D}_{el} is the first matrix given in equation 8 and \mathbf{D}_{visc} is the second matrix given in equation 8. Equation 9 is substituted into equation 1 to yield the total equations of motion:

$$\rho^{s,f} \ddot{\mathbf{u}} = \mathbf{B}^T \mathbf{D}_{el} \mathbf{B} \tilde{\mathbf{u}} + \mathbf{B}^T \mathbf{D}_{visc} \dot{\tilde{\mathbf{u}}}. \quad (10)$$

Geometrical model

To simulate SGWs and their behavior at a crack tip, the three model setups sketched in Figure 1 are used. The first model (labeled 1)

consists of a straight horizontal crack of thickness $h = 3$ mm that runs through the whole model domain and is centered at $y = 0$. This model does not contain a crack tip. The SGW propagates undisturbed along the crack and can be compared with the analytical solutions for the phase velocity (Ferrazzini and Aki, 1987; Korneev, 2008). The second model (labeled 2) consists of half a crack that has an elliptical shape with a horizontal major semiaxis $L = 0.5$ m and a vertical minor axis $h = 3$ mm. The tip of the crack is located at $x = 0$ and $y = 0$. The third model (labeled 3) consists of a straight horizontal crack of length $L = 0.5$ m and thickness $h = 3$ mm, ending at a flat crack tip (i.e., rectangular crack geometry). The tip of the crack is located at $x = 0$ and $y = 0$. In both the second and the third model,

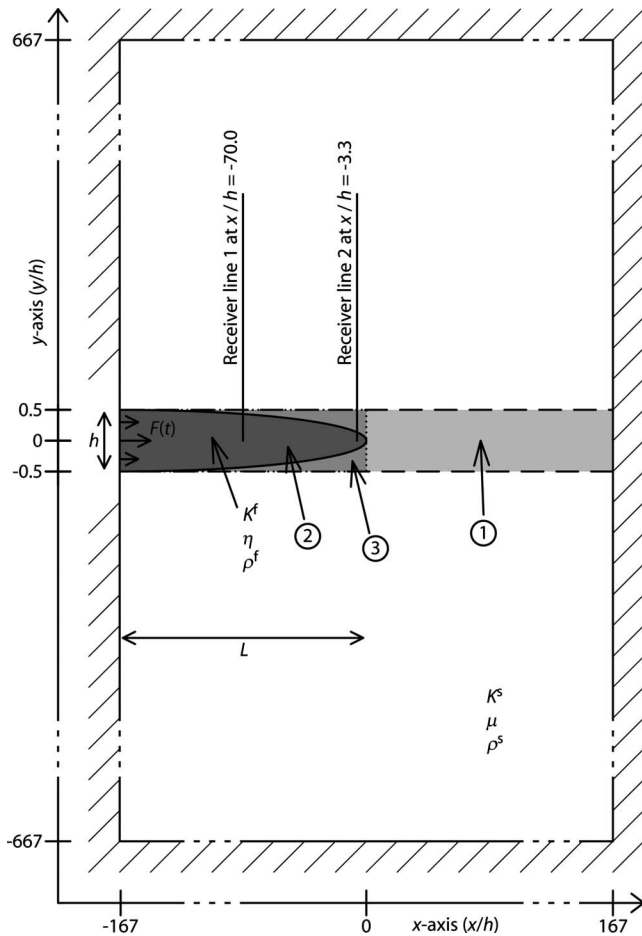


Figure 1. Sketches of the three model setups (labeled 1 to 3) used for 2D numerical simulations: A crack filled with a fluid is surrounded by an elastic rock. The sketches are not to scale and the aspect ratio of the figure is not correct for visualization reasons, i.e., the crack thickness appears much larger than it actually is. All lengths are normalized with the crack thickness h . Model 1 (dashed line) is of a straight horizontal crack with constant thickness $h = 3$ mm that runs through the whole model domain. Model 2 (solid line) represents half a crack that has an elliptical shape and ends inside the model domain. Model 3 (stippled line) represents a rectangular crack with constant thickness $h = 3$ mm that ends inside the model domain at a flat crack tip. In all models, two virtual vertical receiver lines are placed in the positive y -direction. Hatched walls represent the rigid-wall boundary conditions applied all around the model except for the position where the crack is in contact with the left boundary. There, time-dependent boundary conditions, indicated with three arrows, act as the external source.

the SGW propagates along the crack and is partly reflected at the crack tip. In all three model setups, two vertical lines with virtual receivers recording the displacement field are located at $x/h = -70.0$ (line 1) and $x/h = -3.3$ (line 2), respectively. Because all model setups are symmetric around $y = 0$, receivers are only positioned in the positive y -direction.

In all three models, the boundaries are far enough away from the crack to avoid boundary effects. Rigid wall boundary conditions (all displacements $\mathbf{u} = 0$) are applied all around the model except for the position where the crack is in contact with the left boundary. There, only the displacement in the y -direction is forced to vanish and the displacement in the x -direction is prescribed by the time- and space-dependent boundary condition

$$F(t,y) = -A_0 \frac{2(t-t_0)}{\tau^2} \exp\left\{-\frac{(t-t_0)^2}{\tau^2}\right\} \left[1 - \left(\frac{2|y|}{h}\right)^2\right] \quad \text{for } -h/2 \leq y \leq h/2 \text{ and } x = -L, \quad (11)$$

which acts as the external driving force. Equation 11 implies that the source initiating the SGW is located inside the crack. The time-dependent part of $F(t,y)$ is the first derivative of a Gaussian, centered at time t_0 . The space-dependent part of $F(t,y)$ is a hyperbola with maximum amplitude 1 at $y = 0$ and zero amplitude at $y = \pm h/2$. The applied parameters are $A_0 = 10^{-2}$ m, $\tau = 5 \times 10^{-5}$ s, and $t_0 = 2 \times 10^{-4}$ s. This external source contains all frequencies with a central frequency $f_0 = 4500$ Hz. This central frequency may seem high in the context of exploration seismology. But, on one hand, the central frequency used here is not meant to be realistic for a source used in exploration seismology. Rather, it reflects the fast opening or propagation of a crack. On the other hand, the resonance frequency of an SGW propagating back and forth along a finite crack depends on the wave velocity while the length of the crack, and the central frequency is a function of the applied source. The central frequency of the source was deliberately defined relatively high to be distinguishably different from the possible resonance frequency of the SGW.

MODEL PROPERTIES

For the second and third model setups (Figure 1), the aspect ratio of the crack is $(2L)/h = 333$. In this study, the elastic rock always has the same properties and different fluids are defined to fill the crack. Table 1 lists the material parameters of the individual media. Properties for the elastic rock and for water, oil, and hydrocarbon gas agree with values of Ferrazzini and Aki (1987), Mavko et al. (2003), and Korneev (2008). Table 2 lists the properties of the whole model (i.e., fluid-filled crack and surrounding rock) and of the SGW. For comparison, the two dimensionless parameters C (crack stiffness) and F (viscous damping loss) defined by Chouet (1988) as

$$C = \frac{K^f 2L}{\mu h} \quad (12)$$

and

$$F = \frac{12\eta 2L}{\rho^f h^2 V_p^s} \quad (13)$$

are given in Table 2. Formulas for calculating phase velocities of the SGW in Table 2 are given by Ferrazzini and Aki (1987) and Korneev (2008) for inviscid and viscous fluids, respectively, and are not repeated here. For the chosen material parameters, according to Korneev (2008), the model setup lies in the thick fracture regime (see Equation 38 of Korneev, 2008). Also, for the setup with an elliptical crack geometry (i.e., variable crack thickness), at least 99% of the crack lies in the thick fracture regime. Only very close to the tip, the crack becomes more narrow and eventually lies in the thin fracture regime.

To normalize the different wavelengths in the system, crack thickness h can be used. For example, the applied material and source parameters lead to a ratio of $\lambda_{p0}^s/h = 170$, where λ_{p0}^s is the wavelength of a P-wave propagating in the elastic solid with the central frequency of the external source. This shows that the crack is two orders of magnitudes thinner than the wavelength of a P-wave in the surrounding rock. The phase velocity of the SGW is a function of the elastic and viscoacoustic parameters of the rock and the fluid filling the crack, as well as the crack thickness and frequency. Dispersion curves for both inviscid and viscous fluids (Ferrazzini and Aki,

Table 1. Elastic and viscoacoustic material parameters for the different media used in this study. Superscripts s and f denote properties of the elastic rock (solid) and of the fluid, respectively. The dispersive P- and S-wave phase velocity for viscous fluids V_p^f and V_s^f and the corresponding quality factor Q_p^f is calculated for the central frequency of the external source. The low-frequency limit of V_p^f (called V_C) is equal to V_p^f for an inviscid fluid. The S-wave in the viscous fluid exist exclusively due to viscosity and has a diffusive propagation type. The corresponding quality factor Q_s^f is equal to zero. The P- and S-wave phase velocity for the elastic rock is not dispersive and the corresponding quality factors Q_p^s and Q_s^s are infinitely large.

Medium	Solid rock (superscripts)	Water	Oil	Gas
Bulk modulus K (GPa)	5	2.2	1.3	0.022
Ratio K/K^s	1	0.44	0.26	0.0044
Shear modulus μ (GPa)	6	—	—	—
Shear viscosity η (Pa.s)	—	1×10^{-3}	1×10^{-2}	2×10^{-5}
Ratio η/η^{water}	—	1	10	0.02
Density ρ (kg/m ³)	2500	1000	800	100
Ratio ρ/ρ^s	1	0.4	0.32	0.04
P-wave phase velocity V_p (m/s)	2280	1483	1275	469
Ratio V_p/V_p^s	1	0.65	0.56	0.21
Low-frequency limit of $V_p^f = V_C$ (m/s)	—	1483	1275	469
Ratio V_C/V_p^s	—	0.65	0.56	0.21
Quality factor of P-wave in viscous fluid Q_p^f	—	5.8×10^7	3.4×10^6	2.9×10^7
S-wave phase velocity V_s (m/s)	1550	0.238	0.841	0.106
Ratio V_s/V_p^s	0.68	1.0×10^{-4}	3.7×10^{-4}	0.5×10^{-4}

Table 2. Properties of the crack and of the SGW for different fluids that fill the crack. Superscripts s and f denote properties of the elastic rock (solid) and of the fluid, respectively. All properties are calculated for the particular values for the crack geometry, the material properties of the solid and the central frequency of the external source used in this study. The phase velocity of the SGW is calculated using the solutions of Ferrazzini and Aki (1987) and Korneev (2008) for inviscid and viscous fluids, respectively.

Type of fluid	Water	Oil	Gas
Crack stiffness $C = (2K^f L)/(\mu h)$	122	72	1.2
Viscous damping loss $F = (12\eta 2L)/(\rho^f h^2 V_p^s)$	5.8×10^{-4}	73.1×10^{-4}	1.1×10^{-4}
Phase velocity of SGW for viscous fluids V_{SGW} (m/s)	586	609	460
Ratio V_{SGW}/V_p^s	0.26	0.27	0.20
Ratio V_{SGW}/V_p^f	0.40	0.48	0.98
Phase velocity of SGW for inviscid fluid $V_{SGW}^{\text{inviscid}}$ (m/s)	587	611	460
Ratio $V_{SGW}^{\text{inviscid}}/V_p^s$	0.26	0.27	0.20
Ratio $V_{SGW}^{\text{inviscid}}/V_C$	0.40	0.48	0.98
Quality factor of SGW Q_{SGW}	528	144	1189

1987; Korneev, 2008) show a decrease of the phase velocity for low frequencies. For zero frequency, the phase velocity is zero. The high-frequency limit of the phase velocity of the SGW is that of a Scholte wave (Carcione and Helle, 2004), which is the interface wave at a single fluid-solid interface.

Figure 2 shows the phase velocity and Figure 3 the quality factor of the SGW propagating along a straight crack (first model in Figure 1) for a range of material parameters of the fluid, together with the parameters used in this study (Table 1) for constant material parameters of the solid and constant values of h and f_0 . Analytical formulas for producing Figures 2 and 3 are given by Ferrazzini and Aki (1987) and Korneev (2008) for inviscid and viscous fluids, respectively, and are not repeated here. For material parameters of water, oil and hydrocarbon gas, the absolute phase velocity V_{SGW} for inviscid fluids (Figure 2a) lies within a very narrow range of 0.2 to 0.27 times of the P-wave phase velocity in the elastic solid V_p^s . However, compared to the acoustic P-wave phase velocity in the inviscid fluid V_c , the phase velocity of the SGW varies considerably for the different fluids (from $0.4 \times V_c$ for water to $0.98 \times V_c$ for hydrocarbon gas). Plotting the fluid parameter ρ^f versus K^f for water, oil, and hydrocarbon gas results approximately in a straight line in double logarithmic representation (gray line in Figure 2a). This straight line is used as the abscissa in Figure 2b and Figure 3 where the ordinate is the normalized viscosity of the fluid. The viscosities of water, oil, and hydrocarbon gas are too small to have a significant effect on the phase velocity of the SGW compared to the inviscid case (bottom of Figure 2b). At the same time, the quality factor of the SGW (Figure 3) is relatively large (more than 100) for the applied fluid viscosities and only very little attenuation of the SGW is expected.

NUMERICAL METHOD

The algorithm used for numerical simulations is an extended version of the algorithm presented and benchmarked in Frehner et al. (2008). It employs the finite-element method (FEM) (Hughes, 1987; Bathe, 1996; Zienkiewicz and Taylor, 2000) for discretization of the spatial derivatives in equation 10. The particular finite element used is a seven-node isoparametric triangular element with biquadratic continuous interpolation functions (Zienkiewicz and Taylor, 2000). The unstructured numerical mesh is generated by the software Triangle (Shewchuk, 1996; Shewchuk, 2002). It is generated in such a way that interfaces between different media coincide with element boundaries of the finite-element mesh. Figure 4 shows two subfigures on different scales of the same finite-element mesh that discretizes the model setup with the elliptical crack. The finite-element algorithm used comprises the Galerkin weighted-residual method (Zienkiewicz and Taylor, 2000), lumped mass matrix (Bathe, 1996; Cohen, 2002), and Gauss-Legendre quadrature on seven integration points (Zienkiewicz and Taylor, 2000). Equation 10, discretized in space with the FEM, takes the form

$$\mathbf{M}_L \ddot{\mathbf{u}} + \mathbf{C} \dot{\mathbf{u}} + \mathbf{K} \mathbf{u} = 0, \quad (14)$$

where \mathbf{M}_L , \mathbf{C} , and \mathbf{K} are the lumped mass matrix, the damping matrix, and the stiffness matrix, respectively. Displacement vector \mathbf{u} contains the unknown displacements u_x and u_y at all discrete positions in the finite-element mesh. Note that the symbol \sim has been removed from \mathbf{u} compared to equation 10 because it is now discretized in space (i.e., \mathbf{u} contains only the values at numerical nodes). Time derivatives are discretized with an implicit version of the Newmark

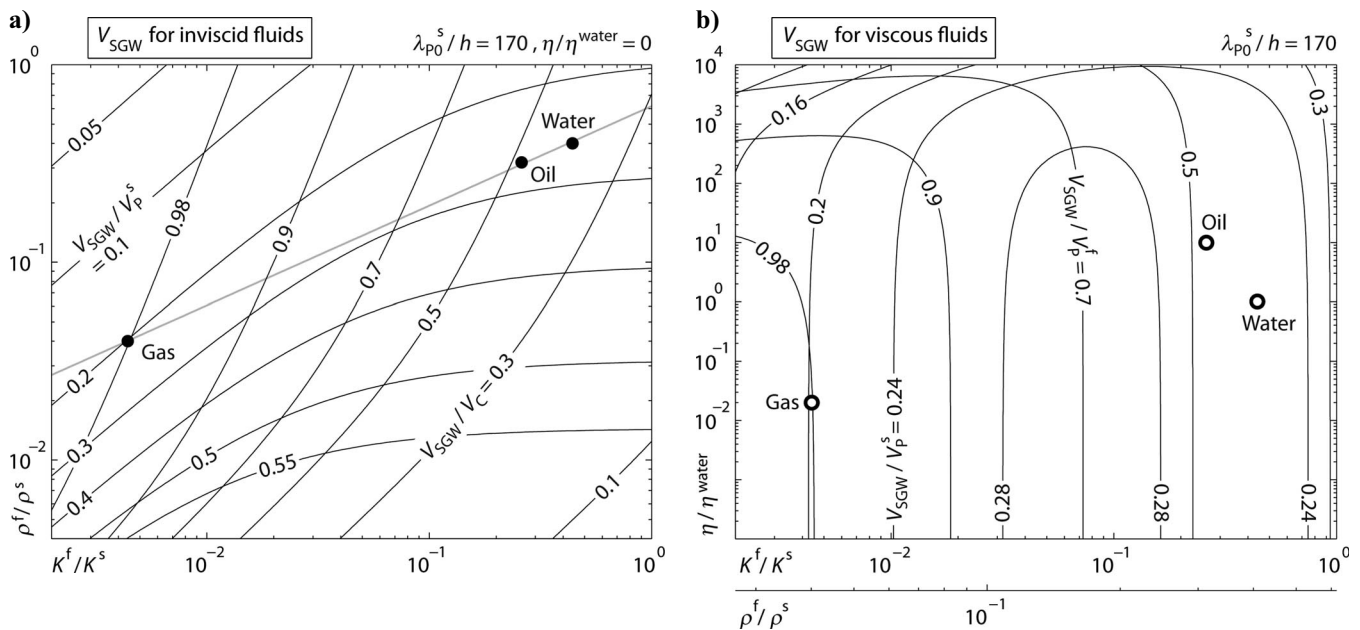


Figure 2. (a) Contour lines of the SGW phase velocity V_{SGW} for a range of acoustic material parameters of the fluid and for zero viscosity (inviscid fluids). (b) Contour lines of the SGW phase velocity V_{SGW} for a range of viscoacoustic parameters of the fluid. The abscissa of (b) is a linear relationship between $\log_{10}(\rho^f)$ and $\log_{10}(K^f)$ that approximately connects the material parameters ρ^f and K^f of water, oil, and hydrocarbon gas and is shown in (a) as a gray line. In both (a) and (b), V_{SGW} is divided by the P-wave phase velocity in the elastic rock V_p^s and by the P-wave phase velocity in the viscoacoustic fluid V_p^f (V_c for the inviscid case in (a)). Material parameters of the solid, the crack thickness h , and the central frequency of the waves f_0 are constant in both (a) and (b). Material parameters of the inviscid (acoustic) and viscoacoustic fluids used in this study (water, oil, and hydrocarbon gas) are indicated as full and open circles, respectively.

algorithm (Zienkiewicz and Taylor, 2000). It is a predictor-corrector algorithm based on a finite-difference formulation:

$$\begin{aligned} \ddot{\mathbf{u}}_{k+1}^{\text{prediction}} &= -\frac{1}{\beta\Delta t^2}\mathbf{u}_k - \frac{1}{\beta\Delta t}\dot{\mathbf{u}}_k - \frac{1-2\beta}{2\beta}\ddot{\mathbf{u}}_k, \\ \text{Predictor: } \dot{\mathbf{u}}_{k+1}^{\text{prediction}} &= -\frac{\gamma}{\beta\Delta t}\mathbf{u}_k + \left(1 - \frac{\gamma}{\beta}\right)\dot{\mathbf{u}}_k + \left(1 - \frac{\gamma}{2\beta}\right)\Delta t\ddot{\mathbf{u}}_k; \end{aligned} \quad (15)$$

$$\begin{aligned} \text{Solution: } \mathbf{u}_{k+1} &= -\left(\frac{1}{\beta\Delta t^2}\mathbf{M}_L + \frac{\gamma}{\beta\Delta t}\mathbf{C} + \mathbf{K}\right)^{-1} \\ &\quad \times (\mathbf{C}\dot{\mathbf{u}}_{k+1}^{\text{prediction}} + \mathbf{M}_L\ddot{\mathbf{u}}_{k+1}^{\text{prediction}}); \end{aligned} \quad (16)$$

$$\begin{aligned} \ddot{\mathbf{u}}_{k+1} &= \ddot{\mathbf{u}}_{k+1}^{\text{prediction}} + \frac{1}{\beta\Delta t^2}\mathbf{u}_{k+1}, \\ \text{Corrector: } \dot{\mathbf{u}}_{k+1} &= \dot{\mathbf{u}}_{k+1}^{\text{prediction}} + \frac{\gamma}{\beta\Delta t}\mathbf{u}_{k+1}; \end{aligned} \quad (17)$$

Subscript k is the index of any discrete time interval and Δt is the time increment. For the two Newmark parameters β and γ , the optimal values of $\frac{1}{4}$ and $\frac{1}{2}$ are chosen (Newmark, 1959; Bathe, 1996). Because the time integration method is implicit, no stability criterion for the time increment has to be fulfilled and the time increment Δt can be chosen independently from the spatial resolution. This allows having a very fine spatial resolution (Figure 4) without the need of a very small time increment. The time increment is chosen in such a way that a P-wave in the elastic rock travels the distance $2L$ in 2000 time steps. Spatial resolution is chosen in such a way that the wavelength of the SGW wave is resolved with at least 80 numerical

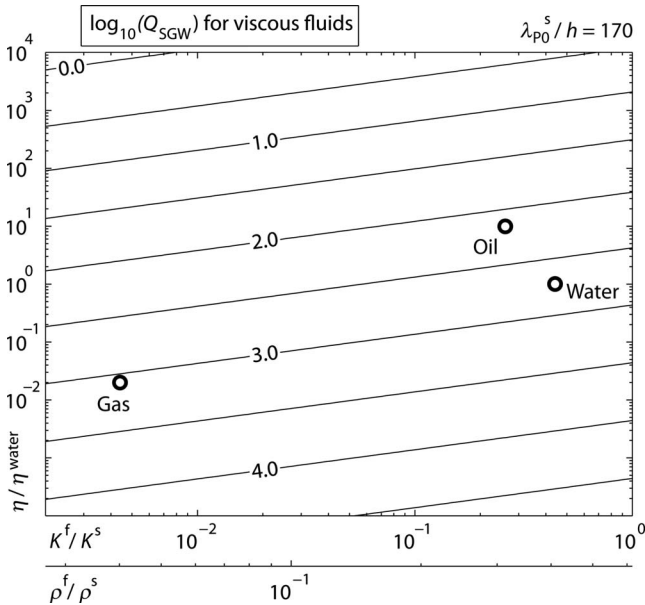


Figure 3. Contour lines of the logarithm of the quality factor of the SGW Q_{SGW} for a range of viscoacoustic parameters of the fluid. The abscissa is a linear relationship between $\log_{10}(\rho^f)$ and $\log_{10}(K^f)$ that approximately connects the material parameters ρ^f and K^f of water, oil, and hydrocarbon gas and is shown in Figure 2a as a gray line. Material parameters for the solid, the crack thickness h , and the central frequency of the waves f_0 are kept constant. Material parameters of the viscoacoustic fluids used in this study (water, oil, and hydrocarbon gas) are indicated as open circles.

points. Propagation velocity of the very slow diffusion-type S-wave in the viscous fluid (i.e., diffusion velocity) is orders of magnitude lower than all other waves in the model (see Table 1). Therefore, for the simulated time span, the S-wave in the fluid is quasi-stationary. However, the most important effect of viscosity, i.e., the damping of all the different propagating waves, is correctly simulated in the model. The numerical algorithm is written in MATLAB and the system of equations is solved with a standard direct solver provided by MATLAB. Simulations were performed on one CPU on a standard workstation. The FEM for wave propagation also can be used in combination with explicit finite-difference time-integration schemes or with finite-element time-integration schemes. Different schemes are presented and compared in Frehner et al. (2008).

Benchmark of the numerical code

A modified version of the numerical code is benchmarked in Frehner et al. (2008) for a different geometrical setup comprising fully elastic and acoustic media but no viscoacoustic media. Figure 5 shows the phase-velocity dispersion curves of an SGW calculated for a straight crack and for the model parameters displayed in the figure. Analytical solutions are taken from Ferrazzini and Aki (1987) and Korneev (2008) for acoustic (inviscid) and viscoacoustic fluids, respectively. Five numerical simulations were performed with different central frequencies of the external source. The model consist-

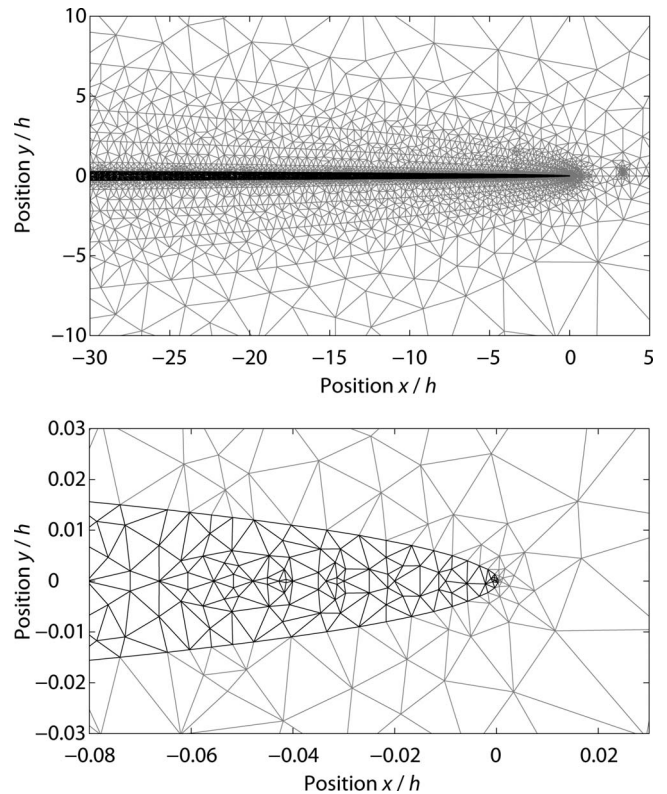


Figure 4. Two subfigures on different scales of the same numerical finite-element mesh discretizing the model with the elliptical crack (second model in Figure 1). Black elements have material parameters of the viscoacoustic fluid. Gray elements have material parameters of the elastic rock. The spatial resolution of the mesh varies strongly, being very fine inside and close to the crack. In both subfigures, it is not possible to show the entire crack and the entire numerical mesh because the numerical domain is much larger.

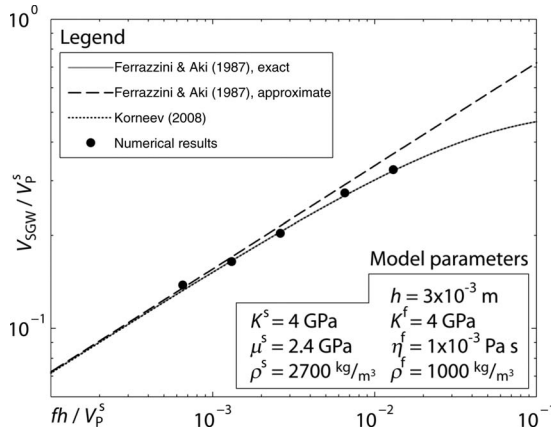


Figure 5. Phase velocity dispersion curve for an SGW propagating along a straight crack for the displayed model parameters. Ferrazzini and Aki (1987) provide an exact (their equation 14b) and an approximate (their equation 16, also presented in equation 1 in Korneev, 2008) solution for an infinite crack filled with an inviscid (acoustic) fluid. In his equation 40, Korneev (2008) provides a solution for a crack filled with a viscoacoustic fluid. Numerical results are derived from five simulations using the first model in Figure 1 with different central frequencies f_0 in the external source. The phase velocity of the SGW V_{SGW} is normalized with the phase velocity of a P-wave in the rock V_P^s . The frequency f is normalized with V_P^s/h .

ing of a straight crack (Figure 1, first model) is used for comparison with the analytical solutions. The velocity of the SGW calculated from the time shift between measurements at the two receiver lines (Figure 1) is plotted on top of the analytical solutions. These numerically calculated velocities agree well with the analytical solutions. Because the rest of the study considers only the thick fracture regime defined by Korneev (2008), the benchmark is performed only for this regime.

NUMERICAL RESULTS

In the following, results of the propagation, reflection, and scattering of SGWs are presented that are derived from different numerical simulations.

Radiation of elastic body waves from the crack tip

The SGW is bound to the crack and cannot propagate further when the crack ends. It must be (partly) reflected at the crack tip. Figure 6 shows the snapshots of a simulation of an SGW propagating from left to right along an elliptical crack (second model in Figure 1) filled with viscous water. Panels (a) and (b) show the incident SGW, which is almost unaffected by the presence of the crack tip. Because the crack thins towards the crack tip due to its elliptical shape, the SGW slows down toward the crack tip. Therefore, even though the

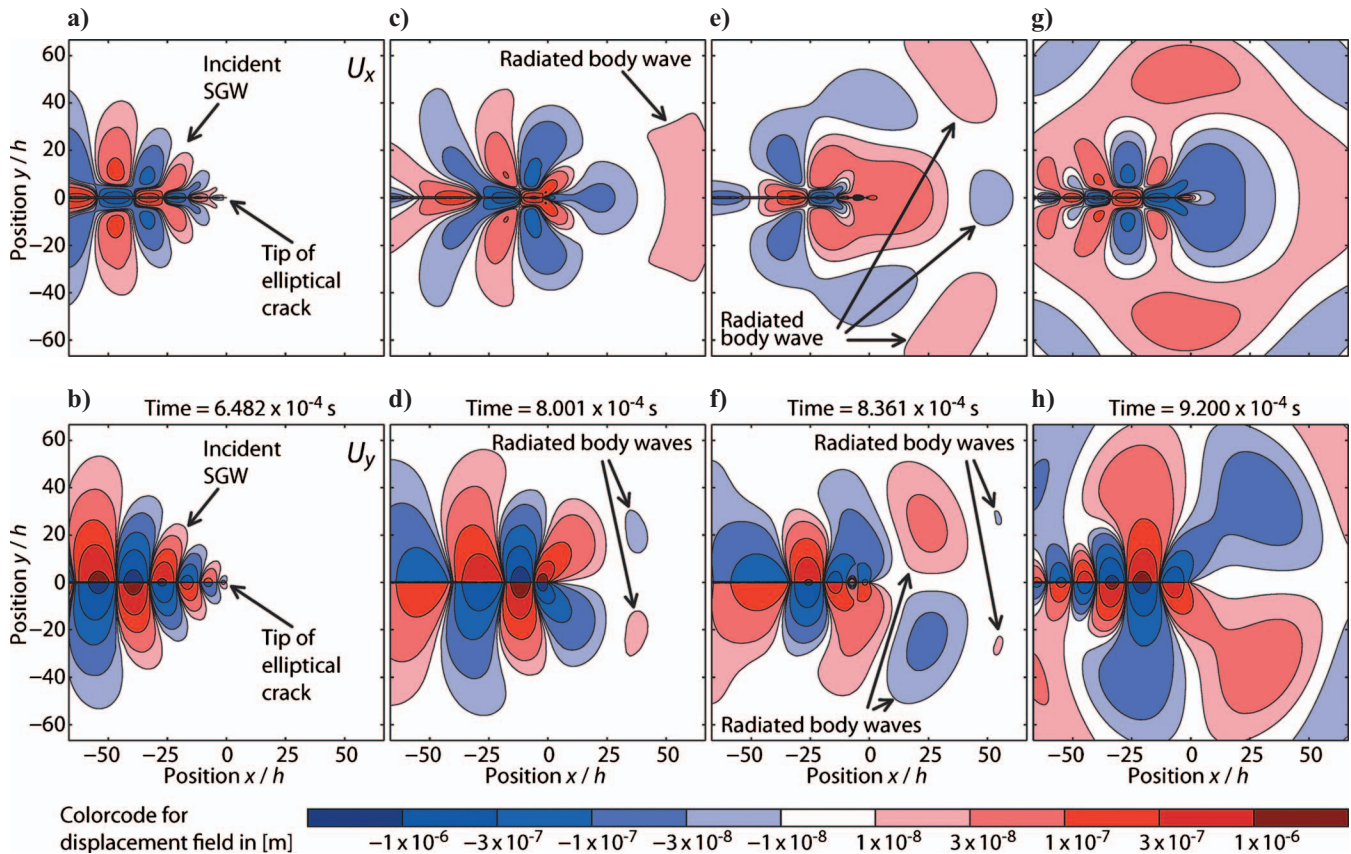


Figure 6. Snapshots of the 2D displacement field of a simulation of an SGW propagating along an elliptical crack (second model in Figure 1) filled with viscous water. Contour lines are defined at values $\pm 1 \times 10^{-8}$ m, $\pm 3 \times 10^{-8}$ m, $\pm 1 \times 10^{-7}$ m, $\pm 3 \times 10^{-7}$ m, and $\pm 1 \times 10^{-6}$ m. Upper panels show the x-component of the displacement field u_x . Lower panels show the y-component of the displacement field u_y . Panels from left to right represent progressive points in time, with time indicated between the panels. Axis labels are only given in the left and lower panels but are valid for all panels. The SGW is partially reflected at the crack tip and elastic body waves are emitted from the crack tip into the surrounding rock.

SGW has not reached the crack tip yet, it is slightly deformed at its front. The regular spacing of the logarithmically plotted contour lines demonstrates the exponential decay of the amplitude away from the crack (Ferrazzini and Aki, 1987). The amplitude decays more than one order of magnitude within one wavelength of the SGW. Panels (c) and (d) show the SGW as it starts being reflected at the crack tip. Also, a part of the wave energy is transferred to the surrounding elastic rock in the form of body waves. The part of the body wave in panel (c) propagating parallel to the crack away from the crack tip (i.e., along the line $y = 0$) is a P-wave because the displacement direction and the propagation direction are parallel. All other visible body waves propagating with a certain angle to the crack away from the crack tip are combinations of P- and S-waves. The exact geometry of the P- and S-waves is not calculated from the displacement field and is not displayed here. In panels (e) and (f), the incident and reflected wavetrains of the SGW interfere destructively and the amplitude close to the crack tip is relatively small. Panels (g) and (h) show the final phase of the reflection process. The SGW now propagates from right to left away from the crack tip.

Interestingly, the radiation pattern of the body waves around the crack tip point in every direction from the crack tip, which leads to the interpretation that the crack tip acts like a point diffractor for the SGW. This interpretation can be understood because the width of the crack and, therefore, the size of the crack tip, are orders of magnitudes smaller than the wavelength of the SGW. In all panels of Figure 6, the interference of the incoming and reflected SGW trains leads to a node (zero amplitude) exactly at the crack tip. Therefore, the re-

flection pattern of the SGW can be compared to a reflection of a 1D wave propagating in a medium with lower impedance at the interface to a medium with higher impedance.

Figure 7 shows snapshots of a simulation of an SGW propagating from left to right along a straight crack with a flat crack tip (third model in Figure 1) filled with viscous water. Unlike in Figure 6, the phase velocity of the SGW does not change along the crack due to the constant thickness of the crack. Therefore, the individual snapshots in Figure 7 are not displayed for the same points in time as in Figure 6 but it was tried to display the same stages of the reflection process to make Figures 6 and 7 comparable. The reflection pattern of the SGW at the flat crack tip is very similar to the one at the elliptical crack tip. However, the wavetrain is not compressed towards the crack tip because the SGW does not slow down towards the crack tip. Similar to the elliptical crack tip, the radiation pattern of body waves around the flat crack tip point in every direction from the crack tip at the end of the reflection process. However, a major difference between the two geometrical setups is the amplitudes of these body waves in the elastic solid, with the amplitudes being considerably higher for a flat crack tip.

Reflection of the SGW at the crack tip

As seen above, not all of the wave energy of the SGW is reflected at the crack tip but a part is radiated into the surrounding rock in the form of elastic body waves. Figure 8 displays the displacement-time signal at two receivers on receiver line 1 (Figure 1), one inside and one outside the crack, for a simulation of an SGW being reflected at

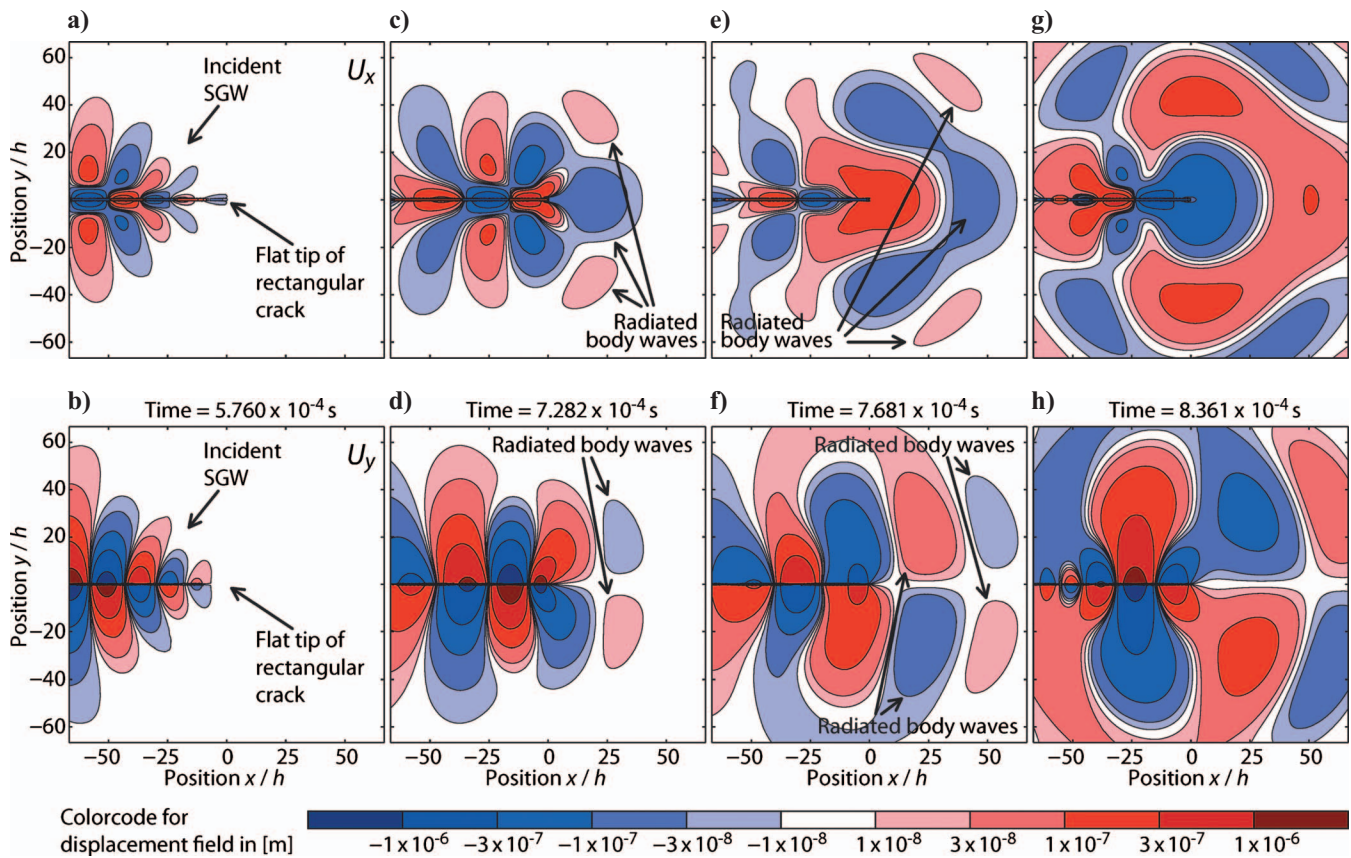


Figure 7. Same as Figure 6 but for a rectangular crack with a flat crack tip (third model in Figure 1). Note that the time of the snapshots is not the same as in Figure 6 because the SGW travels with a slightly different velocity.

the tip of an elliptical crack (second model in Figure 1) filled with viscous water. The incident and reflected SGWs are well separated from each other in time. To quantify the reflected part of the SGW, Figure 9 shows the amplitude ratio R between reflected and incident SGW for different model setups and for different fluids filling the crack. Here, the term reflection coefficient is avoided because not only the amplitude changes but also the shape of the SGW when it is reflected. Values of R are calculated from the displacement-time signals at receivers on receiver line 1 (Figure 1), like the example shown in Figure 8. For each simulation two values for R are calculated, one at receivers inside the crack in the viscoacoustic fluid and one for receivers outside the crack in the elastic rock. Values labeled “oil with gas cap, elliptical crack tip” are discussed later. Values plotted for material properties of water (values to the right of Figure 9) correspond to the two simulations shown in Figures 6 and 7. The amplitude of the SGW reflected at the tip of an elliptical crack filled with water is around 77% of the amplitude of the incident crack and only around 43% when reflected at the flat crack tip. This is remarkable because the size of the crack tip is orders of magnitude smaller than the wavelength of the SGW but still has a big impact.

The difference in reflection behavior also explains the amplitude difference of the radiated body waves shown in Figures 6 and 7. The part that is not reflected is radiated into the surrounding rock. Therefore, a stronger reflection (elliptical crack) leads to smaller amplitudes of the radiated body waves. For different fluids filling the elliptical crack, the reflection is also different. Hydrocarbon gas leads to the strongest reflection with R of almost 100%. This also means that from a crack filled with hydrocarbon gas, only small-amplitude body waves are radiated when the SGW is reflected at the crack tip. An SGW propagates both in the fluid that fills the crack and in the rock surrounding the crack. It is therefore unclear how to calculate the impedance for an SGW. However, the strong reflection for a crack filled with hydrocarbon gas can be qualitatively understood by considering the impedance of the P-wave in the fluid ($\sqrt{K^f \rho^f}$), which is much smaller for hydrocarbon gas than for water and oil. Therefore, the impedance contrast to the surrounding rock is much bigger, which leads to a strong reflection.

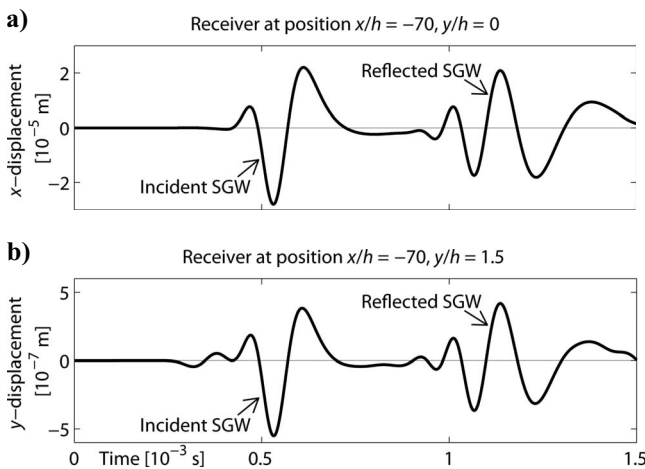


Figure 8. (a) Displacement-time signal in the x -direction at a receiver inside the crack on receiver line 1 (Figure 1). (b) Displacement-time signal in the y -direction at a receiver outside the crack on receiver line 1. Both traces are obtained from a simulation of an SGW propagating along an elliptical crack (second model in Figure 1) filled with viscous water. Labels for the time axis are only given in (b) but are valid for (a) also.

Due to the interference between incident and reflected SGWs, the amplitudes add up close to the crack tip. Figure 10 shows this effect and how the amplitude decays away from the crack along receiver line 2 (see Figure 1) for different model setups and different fluids filling the crack. The amplitude distribution shows the same exponential decay as discussed in Ferrazzini and Aki (1987). As a reference (solid gray line), the amplitude decay along receiver line 1 for an elliptical crack filled with water is also given in Figure 10. For this case, the wavelength of the SGW is around 40 times the crack thickness h . At this distance away from the crack, the amplitude decay is more than an order of magnitude. The amplitude at the crack interface at receiver line 2 for a water — or oil-filled crack is increased by about 30% due to the interference between incident and reflected SGWs. Also, the two crack geometries (elliptical and rectangular crack) that are filled with water do not influence this factor significantly. The same amplitude for a crack filled with hydrocarbon gas is increased by about 120%. This is remarkable because for a reflection as strong as $R = 100\%$ (Figure 9), a maximal increase in amplitude close to the crack tip of 100% is expected. However, the wave velocity of the SGW also decreases towards the crack tip due to the elliptical shape of the crack. This lets the amplitude of the SGW further increase, which adds up to the maximal 100% increase in amplitude due to the reflection process. For all cases shown in Figure 10, even though the amplitude at the crack interface is increased, the exponential decay away from the crack happens within a relatively short

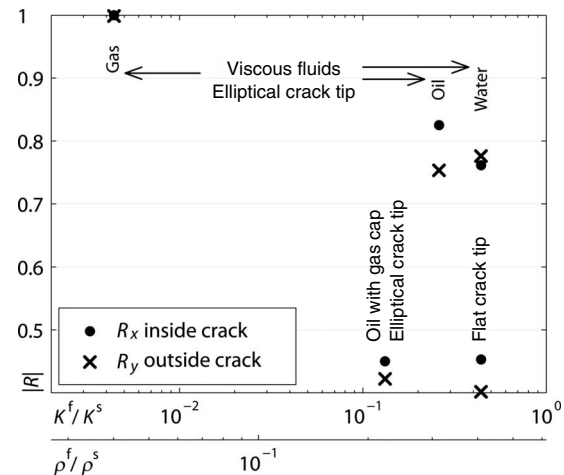


Figure 9. Absolute value of the amplitude ratio $|R|$ between reflected and incident SGW of an SGW that is reflected at the tip of a crack. The abscissa is the same as in Figure 2b and Figure 3. R_x is calculated from the displacement-time signals in the x -direction of eight receivers inside the crack on receiver line 1 at position $y/h = 0$ to 0.35. R_y is calculated from the displacement-time signals in the y -direction of six receivers outside the crack on receiver line 1 at position $y/h = 0.45$ to 5.5. Values labeled “viscous fluids, elliptical crack tip” are derived from simulations of an elliptical crack (second model in Figure 1) fully saturated with the corresponding viscous fluid. Values labeled “flat crack tip” are derived from a simulation of a rectangular crack with a flat crack tip (third model in Figure 1) fully saturated with viscous water. Values labeled “oil with gas cap, elliptical crack tip” are derived from a simulation of an elliptical crack (second model in Figure 1) partially saturated with viscous oil and having a small gas cap at the crack tip. These values are plotted at $(K^{\text{Oil}} + K^{\text{Gas}})/2$. All values of $|R|$ are corrected for the intrinsic attenuation due to viscous damping in the fluids.

distance. For cracks filled with water or oil, the amplitude along receiver line 2 is even smaller than along receiver line 1 for distances greater than five times the crack thickness.

Advanced model setups

The model setup consisting of an elliptical crack (second model in Figure 1) is used for simulating a partially filled crack. The crack is filled with viscous oil and has a small cap at the crack tip filled with hydrocarbon gas. The gas cap extends from $x/h = -31.8$ to $x/h = 0$. Figure 11 shows the snapshots of the displacement field in the x - and y -direction after the SGW is reflected at the crack tip. A major part of the SGW is reflected already at the oil-gas contact line and only a small-amplitude SGW propagates further along the crack where it is reflected at the crack tip. This multiple reflection leads to the complex reflection pattern in Figure 11. One major difference to the crack filled only with oil (almost identical to the crack filled only with water, Figure 6) is the amplitude and radiation pattern of the elastic body waves that are radiated away from the crack tip when the SGW is reflected. The radiation pattern is much more forward-directed towards the propagation direction of the incident SGW, compared to a radiation pattern pointing in every direction for the fully saturated crack (Figure 6). Also, the amplitudes of the radiated body waves are much larger. Figure 9 shows the amplitude ratio R between reflected and incident SGW for both cases. For the crack fully saturated with oil, R is about 78%. It is reduced to about 43% when the gas cap is present. The larger amplitudes of the radiated body waves also mean that less of the energy of the SGW is reflected compared to the fully saturated crack.

Distributed individual and isolated cracks are only one possible crack pattern in nature. More common are probably swarms of similarly oriented cracks or two or more families of cracks whose orientations intersect. Figure 12 shows two snapshots at different points in time of a simulation of two intersecting cracks. The first crack, in which the SGW is initiated, has an aspect ratio of 333. The second

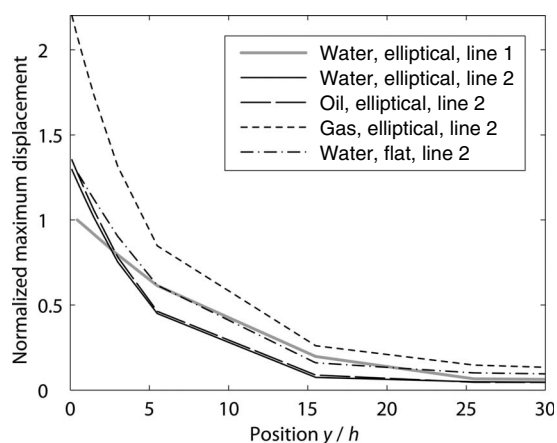


Figure 10. Maximum absolute particle displacement along receiver lines 1 and 2 (Figure 1) recorded during four different simulations. Three simulations are for an elliptical crack filled with three different viscous fluids. The fourth simulation is for a rectangular crack ending at a flat crack tip filled with viscous water. Maximum absolute particle displacement along receiver line 1 is only shown for the elliptical crack filled with water (solid gray line) because it is almost identical for all simulations. All values of one simulation are normalized with the maximum absolute particle displacement at the crack interface at receiver line 1.

crack has an aspect ratio of 95. The angle between the two cracks is 60° . The first snapshot (Figure 12a) is taken before the SGW reaches the intersection point of the two cracks. Two SGW trains propagated away from the external source in the crack. The left wavetrain is already reflected at the left crack tip and now both wavetrains are propagating towards the intersection point to the right. Also visible are the elastic body waves that propagate in the surrounding rock away from the external source and are scattered by the cracks. The second snapshot (Figure 12b) is taken after the first SGW train passed the intersection point of the two cracks. Only a part of the SGW continues propagating straight ahead along the first crack. A part is reflected at the intersection point and interferes with the second SGW train on the first crack. A considerable part of the SGW makes a sharp turn and propagates along the two branches of the second crack. Also, elastic body waves are radiated away from the intersection point into the surrounding rock.

DISCUSSION

Models of SGWs propagating along fluid-filled cracks on various scales are used to explain the occurrence of long-period volcanic tremor (Aki et al., 1977; Chouet, 1988; Chouet, 1996). The magma chamber as a whole or fractures around the volcanic conduit can be considered as the waveguide where an SGW propagates back and forth, which results in a characteristic frequency. Because the SGW amplitude decays exponentially away from the crack, the way this

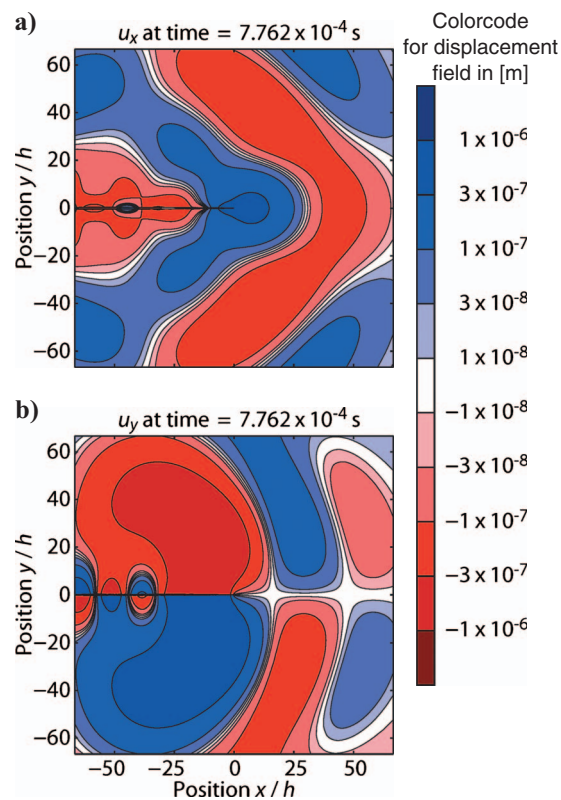


Figure 11. (a) Snapshots of the x - and (b) y -component of the 2D displacement field of a simulation of an SGW propagating along an elliptical crack (second model in Figure 1). The crack is filled with viscous oil and has a small gas cap at the crack tip. Contour lines are the same as in Figures 6 and 7. Axis labels for the abscissa are only given in (b) but are valid in (a) also.

long-period signal is transmitted to recording stations at the earth's surface remained unclear. The emission of elastic body waves discussed in this study makes it possible to detect SGW-related signals even in distances away from the crack where the amplitude of the SGW itself is too small to be measured. Which type of body wave (i.e., P- or S-waves) is more important remains to be determined in a future study. The orientation of fully saturated cracks (or magma chambers) might not be determinable from measurements of volcanic tremor due to the radiation pattern that points in every direction from the crack tip, but it might be possible for cracks containing a gas cap. Depending on the type of magma, viscosities can vary by orders of magnitude, but in general, they are considerably larger than that of the fluids considered in this study. Depending on the magma viscosity and the crack thickness, the quality factor of an SGW lies between 1 and 100. The reflection of an SGW at the tip of a crack can still be strong. However, an SGW in a thin crack filled with a highly viscous magma is expected to be attenuated relatively fast and cannot propagate back and forth along the crack several times. Consequently, no long-period volcanic tremor will be generated. If long-period volcanic tremors are a result of SGWs falling into resonance,

it is more likely to observe them when lower-viscosity magmas are present in thicker cracks. Still, it is unlikely that a single SGW would propagate back and forth along the crack many times and produce a continuous long-period volcanic tremor. For this, a continuous excitation of SGWs would be necessary.

Reservoir rocks for hydrocarbons often contain a large number of fractures. The network of fractures contributes significantly to the permeability of a reservoir. Kostek et al. (1998) and Ionov (2007) demonstrate that fractures can have an important effect in borehole seismology. Also, SGW-related effects (such as rock-internal resonance) can be important for monitoring hydrofracturing processes during the exploration of hydrocarbon reservoirs. However, current models for poroelastic and fractured rocks do not include these effects. This and future studies will help to include SGW-related effects into more realistic models for fractured rocks (Korneev et al., 2009). Frehner et al. (2009) develops a basic model that couples resonance effects with seismic wave propagation. This model was applied to oscillations that can take place on the pore level due to surface-tension effects in partially saturated porous rocks. However, the resonant behavior of SGWs in fractured rocks is another possible explanation for the wave propagation-oscillation model presented in Frehner et al. (2009). Models need to be designed for a whole finite crack where both crack tips are fully resolved to simulate the propagation of SGW back and forth along the crack and the development of the corresponding resonance frequency. Korneev (2009) shows that oscillations in the subsurface can be measured with a seismic array. Oscillations are easier to detect in late arrivals when they are not masked by high-energy body waves. This implies that long-lasting oscillations are more easily detectable than short-lasting oscillations. In the case of an SGW, this means that a strong reflection at the crack tip eventually enables the detection of the resonant character of the SGW.

All presented simulations use a source inside the crack. Possible causes of a source inside the crack are, for example, the opening or propagation of the crack due to magma migration in a volcanic area (Chouet, 1986) or hydrofracturing of a subsurface reservoir that is under production. For a source inside the crack, it is clear that an SGW is initiated. It remains to be determined whether a source outside the crack, e.g., a plane P- or S-wave in the elastic surrounding rock, is capable of initiating an SGW with significant amplitude. This important next step will help to understand how body waves are influenced by SGWs in fractured rocks. Because SGWs can generate resonance in finite cracks, it can be expected that there are frequency-dependent effects on body waves, e.g., attenuation and dispersion. Understanding how strong these effects are is essential for cases where body waves propagate through fluid-saturated fractured rocks, such as in exploration seismology or site effects analysis of earthquake data. Especially in exploration seismology, a better understanding of the resonating SGWs in a fractured reservoir can help to determine fracture-related petrophysical parameters (such as fracture length, fracture orientation, or fluid viscosity).

The presented numerical models deal with a multiscale wave-propagation phenomenon with length scales of different orders of magnitude. Although highly resolved, the numerical setup is still rather simple, consisting of only one single crack. In this study, one approach toward more realistic model setups is shown by modeling two highly resolved intersecting cracks. Another approach is, for example, a model of many cracks (Saenger and Shapiro, 2002; Saenger et al., 2004). The primary investigation target of such models is to determine effective bulk rock properties. However, the high spatial

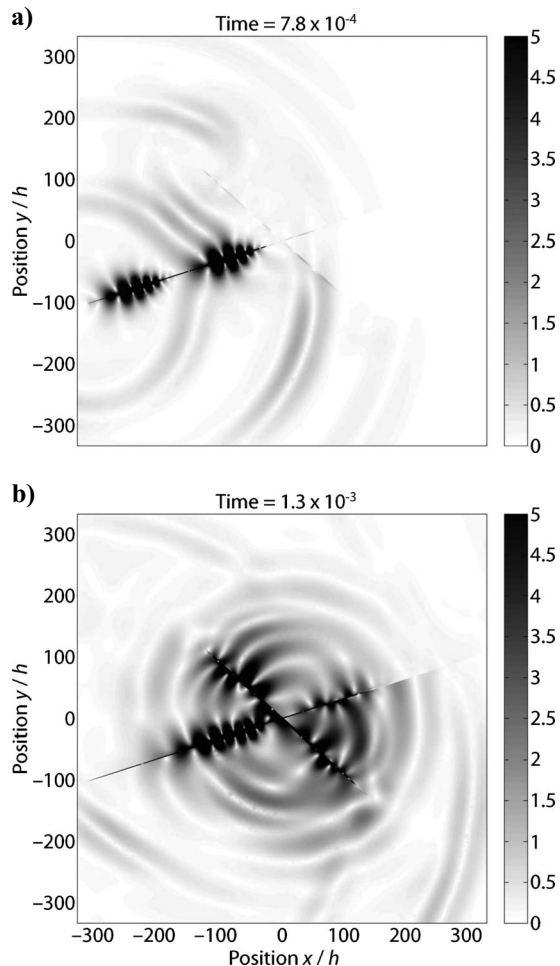


Figure 12. (a and b) Snapshots of the 2D displacement field at two different points in time of a simulation of an SGW propagating along an elliptical crack that is intersected by a second elliptical crack. The displayed value is the normalized absolute particle displacement $10^6 \sqrt{u_x^2 + u_y^2}$. The cracks are filled with viscous water. Axis labels for the abscissa are only given in (b) but are valid in (a) also.

resolution that is needed for accurately modeling SGWs is lacking in these models. For further insight into the significance of SGWs in a realistic fractured rock, both end-member modeling approaches have to be brought together to have a high-resolution model of a fractured rock with a large number of cracks. Also, the presented model needs to be expanded to 3D to cover a larger variety of possible geometries of the crack. Although the 2D plain-strain model is a good approximation of a crack with a relatively round crack surface (i.e., penny-shaped cracks) or a crack with straight edges, a fully 3D model also could handle strongly elongated cracks (i.e., cigar-shaped cracks).

For the chosen model parameters, more than 99% of the simulated crack length is in the thick fracture regime, according to Korneev (2008). It is shown that the crack geometry (elliptical and straight with a flat crack tip) significantly influences the reflection behavior of the SGW. However, the two crack geometries are rather simplistic. More realistic crack geometries can comprise rugose crack surfaces, asymmetric crack geometry, or pinching out of the crack tip (e.g., Barenblatt, 1996). For thinner cracks or for cracks pinching out at the crack tip, a larger part of the crack would lie in the thin fracture regime, according to Korneev (2008). In the thin fracture regime, fluid viscosity plays a more important role and the behavior of the SGW changes considerably. Studies similar to the one presented for the thin fracture regime remain to be done in the future. However, both pinching-out cracks and 3D cracks require a more powerful numerical implementation.

Using the conventional FDM, it is not straightforward to discretize an elliptical crack with the rectangular numerical grid. Staircase-like discretization leads to numerical inaccuracies (Frehner et al., 2008). A logical choice for the crack geometry in FDM-simulations is a straight crack with a flat crack tip (Chouet, 1986; Kostek et al., 1998; Groenenboom and Falk, 2000). Conversely, the FEM can handle both crack geometries with ease because it uses an unstructured numerical mesh. This difference is critical because the two crack geometries have a major influence on the reflection of SGWs and on the amplitude of the radiated elastic body waves. The sharp edges at the tip of the straight crack scatter SGWs much more than the smooth elliptical crack tip.

CONCLUSIONS

SGWs propagate along cracks and are partly reflected at the crack tip. The interference between incident and reflected SGWs leads to a node (zero amplitude) exactly at the crack tip. A relatively short distance away from the crack the SGW amplitude is too small to be detected due to the exponential decay away from the crack. This is true even during the reflection process when the SGW amplitude is increased due to the interference between incident and reflected SGWs.

The reflection of the SGW at the crack tip depends on the fluid properties in the crack and the crack geometry. An elliptical crack having a round tip exhibits a significantly stronger reflection than a rectangular crack having sharp corners at the tip. Elliptical fractures filled with gas, oil, or water exhibit strong reflection with an amplitude ratio between the reflected and the incident SGW ranging between about 75% and almost 100%.

The part of the SGW that is not reflected at the crack tip is emitted into the surrounding elastic rock in the form of body waves. This makes the detection of SGW-related signals possible even away from the crack where the SGW itself cannot be detected. The radia-

tion pattern of these body waves points in every direction from the crack tip for a fully saturated crack. In the presence of a small gas cap at the crack tip, the radiation pattern is predominantly directed in the propagation direction of the incident SGW.

The propagation of SGWs along a crack is a multiscale problem where the different scales need to be resolved in detail. The FEM is a suitable numerical method for simulating such problems. The unstructured numerical mesh allows having a fine resolution where it is needed without the need of a fine resolution elsewhere in the numerical domain. Also, the unstructured mesh allows resolving complex geometries accurately without introducing staircase-like discretization. The very fine spatial resolution would lead to a very small explicit time increment, and therefore to long calculation times. Implicit time integration is a suitable alternative for wave propagation in fluid-filled finite cracks.

ACKNOWLEDGMENTS

Many constructive inputs from Brad Artman, Erik Saenger, Tung Nguyen, Beatriz Quintal, Marc Lambert, and Brian Steiner helped to improve this manuscript. Dani Schmid is acknowledged for providing an algorithm that links the applied finite-element algorithm with the mesh-generator Triangle. Sarah Lechmann is acknowledged for providing computational resources. Helpful comments from three reviewers, especially Valeri Korneev, are greatly acknowledged. This work was supported by the ETH Zurich and cofinanced by Spectraseis AG, Switzerland, and by the Swiss Commission for Technology and Innovation, CTI.

REFERENCES

- Achenbach, J. D., 1973, *Wave propagation in elastic solids*: North-Holland Publishing Company.
- Aki, K., M. Fehler, and S. Das, 1977, Source mechanism of volcanic tremor: Fluid-driven crack models and their application to the 1963 Kilauea eruption: *Journal of Volcanology and Geothermal Research*, **2**, 259–287.
- Aki, K., and P. G. Richards, 2002, *Quantitative seismology*: University Science Books.
- Ashour, A. S., 2000, Wave motion in a viscous fluid-filled fracture: *International Journal of Engineering Science*, **38**, 505–515.
- Barenblatt, G. I., 1996, *Scaling, self-similarity, and intermediate asymptotics*: Cambridge University Press.
- Bathe, K.-J., 1996, *Finite element procedures*: Prentice Hall.
- Biot, M. A., 1962, Mechanics of deformation and acoustic propagation in porous media: *Journal of Applied Physics*, **33**, 1482–1498.
- Bourbie, T., O. Coussy, and B. Zinszner, 1987, *Acoustics of porous media*: Editions Technip.
- Carcione, J. M., 2001, *Wave fields in real media: Wave propagation in anisotropic, anelastic and porous media*: Elsevier.
- Carcione, J. M., and H. B. Helle, 2004, The physics and simulation of wave propagation at the ocean bottom: *Geophysics*, **69**, 825–839.
- Chen, Z. Y., H. Steeb, and S. Diebels, 2008, A new hybrid velocity integration method applied to elastic wave propagation: *International Journal for Numerical Methods in Engineering*, **74**, 56–79.
- Chouet, B., 1986, Dynamics of a fluid-driven crack in three dimensions by the finite-difference method: *Journal of Geophysical Research*, **91**, 13967–13992.
- , 1988, Resonance of a fluid-driven crack: Radiation properties and implications for the source of long-period events and harmonic tremor: *Journal of Geophysical Research*, **93**, 4375–4400.
- , 1996, Long-period volcano seismicity: Its source and use in eruption forecasting: *Nature*, **380**, 309–316.
- Cohen, G. C., 2002, *Higher-order numerical methods for transient wave equations*: Springer Verlag.
- Dvorkin, J., G. Mavko, and A. Nur, 1995, Squirt flow in fully saturated rocks: *Geophysics*, **60**, 97–107.
- Faoro, I., A. Niemeijer, C. Marone, and D. Elsworth, 2009, Influence of shear and deviatoric stress on the evolution of permeability in fractured rock: *Journal of Geophysical Research*, **114**, B01201.

- Ferrazzini, V., and K. Aki, 1987, Slow waves trapped in a fluid-filled infinite crack: Implication for volcanic tremor: *Journal of Geophysical Research*, **92**, 9215–9223.
- Frehner, M., S. M. Schmalholz, and Y. Podladchikov, 2009, Spectral modification of seismic waves propagating through solids exhibiting a resonance frequency: A 1-D coupled wave propagation-oscillation model: *Geophysical Journal International*, **176**, 589–600.
- Frehner, M., S. M. Schmalholz, E. H. Saenger, and H. Steeb, 2008, Comparison of finite difference and finite element methods for simulating two-dimensional scattering of elastic waves: *Physics of the earth and planetary interiors*, **171**, 112–121.
- Groenenboom, J., and J. Falk, 2000, Scattering by hydraulic fractures: Finite-difference modeling and laboratory data: *Geophysics*, **65**, 612–622.
- Higham, N. J., 1996, Accuracy and stability of numerical algorithms: Society for Industrial & Applied Mathematics.
- Hudson, J. A., 1980, Overall properties of a cracked solid: *Mathematical Proceedings of the Cambridge Philosophical Society*, **88**, 371–384.
- , 1981, Wave speeds and attenuation of elastic-waves in material containing cracks: *Geophysical Journal of the Royal Astronomical Society*, **64**, 133–150.
- Hughes, T., 1987, *The finite element method: Linear static and dynamic finite element analysis*: Dover Publications.
- Ionov, A. M., 2007, Stoneley wave generation by an incident P-wave propagating in the surrounding formation across a horizontal fluid-filled fracture: *Geophysical Prospecting*, **55**, 71–82.
- Käser, M., and M. Dumbser, 2008, A highly accurate discontinuous Galerkin method for complex interfaces between solids and moving fluids: *Geophysics*, **73**, no. 3, T23–T35.
- Korneev, V., 2008, Slow waves in fractures filled with viscous fluid: *Geophysics*, **73**, no. 1, N1–N7.
- , 2009, Resonant seismic emission of subsurface objects: *Geophysics*, **74**, no. 2, T47–T53.
- Korneev, V. A., A. A. Ponomarenko, and M. Kashtan, 2009, Stoneley guided waves: What is missing in Biot's theory?, in H. I. Ling, A. Smyth, and R. Betti, eds., *Poromechanics IV: Proceedings of the fourth Biot conference on poromechanics*: DEStech Publications Inc., 706–711.
- Kostek, S., D. L. Johnson, and C. J. Randall, 1998, The interaction of tube waves with borehole fractures, Part I: Numerical models: *Geophysics*, **63**, 800–808.
- Krüger, O. S., E. H. Saenger, and S. A. Shapiro, 2005, Scattering and diffraction by a single crack: An accuracy analysis of the rotated staggered grid: *Geophysical Journal International*, **162**, 25–31.
- Lindsay, R. B., 1960, *Mechanical radiation*: McGraw-Hill, ISBN 0-0703-7844-0.
- Love, A. E. H., 1927, *A treatise on the mathematical theory of elasticity*: Dover Publications.
- Mavko, G., and D. Jizba, 1991, Estimating grain-scale fluid effects on velocity dispersion in rocks: *Geophysics*, **56**, 1940–1949.
- Mavko, G., T. Mukerji, and J. Dvorkin, 2003, *The rock physics handbook: Tools for seismic analysis in porous media*: Cambridge University Press.
- Newmark, N. M., 1959, A method of computation for structural dynamics: *Journal of the Engineering Mechanics Division*, **85**, 67–94.
- Pujol, J. A., 2003, *Elastic wave propagation and generation in seismology*: Cambridge University Press.
- Saenger, E. H., N. Gold, and S. A. Shapiro, 2000, Modeling the propagation of elastic waves using a modified finite-difference grid: *Wave Motion*, **31**, 77–92.
- Saenger, E. H., O. S. Krüger, and S. A. Shapiro, 2004, Effective elastic properties of randomly fractured soils: 3D numerical experiments: *Geophysical Prospecting*, **52**, 183–195.
- Saenger, E. H., and S. A. Shapiro, 2002, Effective velocities in fractured media: A numerical study using the rotated staggered finite-difference grid: *Geophysical Prospecting*, **50**, 183–194.
- Saenger, E. H., S. A. Shapiro, and Y. Keehm, 2005, Seismic effects of viscous Biot-coupling: Finite difference simulations on micro-scale: *Geophysical Research Letters*, **32**, L14310.
- Shames, I. H., and F. A. Cozzarelli, 1997, *Elastic and inelastic stress analysis*: Taylor & Francis.
- Shewchuk, J. R., 1996, Triangle: Engineering a 2D quality mesh generator and Delaunay triangulator, in C. L. Ming, and M. Dinesh, eds., *Applied computational geometry: Towards geometric engineering*: Springer Verlag, 203–222.
- , 2002, Delaunay refinement algorithms for triangular mesh generation: *Computational Geometry*, **22**, 21–74.
- Virieux, J., 1986, P-SV wave propagation in heterogeneous media: Velocity-stress finite-difference method: *Geophysics*, **51**, 889–901.
- Yamamoto, M., and H. Kawakatsu, 2008, An efficient method to compute the dynamic response of a fluid-filled crack: *Geophysical Journal International*, **174**, 1174–1186.
- Zienkiewicz, O. C., and R. L. Taylor, 2000, *The finite element method: Volume 1 (fifth edition): The basis*: Butterworth-Heinemann.